Impact of dose reduction and the use of an advanced model-based iterative reconstruction algorithm on spectral performance of a dual-source CT system: A task-based image quality assessment

Joël Greffier, Djamel Dabli, Aymeric Hamard, Philippe Akessoul, Asmaa Belaouni, Jean-Paul Beregi, Julien Frandon

To cite this version:

Joël Greffier, Djamel Dabli, Aymeric Hamard, Philippe Akessoul, Asmaa Belaouni, et al.. Impact of dose reduction and the use of an advanced model-based iterative reconstruction algorithm on spectral performance of a dual-source CT system: A task-based image quality assessment. Diagnostic and Interventional Imaging, 2021, 102 (7-8), pp.405-412. 10.1016/j.diii.2021.03.002 . hal-03632918

HAL Id: hal-03632918
https://hal.umontpellier.fr/hal-03632918v1

Submitted on 2 Aug 2023

Version of Record: https://www.sciencedirect.com/science/article/pii/S2211568421000619
Manuscript_4d61202a904e96c6bf2eb416ac8d33d0

Impact of dose reduction and the use of an advanced model-based iterative reconstruction algorithm on spectral performance of a dual-source CT system: a task-based image quality assessment

Short title: Dose reduction and advanced model-based iterative reconstruction in dual source CT

Joël Greffier[a*], Djamel Dabli[a], Aymeric Aymard[a], Philippe Akessoul[a], Asmaa Belaouni[a], Jean-Paul Beregi[a], Julien Frandon[a]

[a]Department of Medical Imaging, CHU Nimes, Univ Montpellier, Medical Imaging Group Nimes, EA 2992, 30029 Nîmes Cedex 9, France

* Corresponding author: joel.greffier@chu-nimes.fr

Abstract

Purpose: To assess the impact of dose reduction and the use of an advanced model-based iterative reconstruction algorithm (ADMIRE) on image quality in low-energy monochromatic images from a dual-source dual energy computed tomography CT (DSCT) platform.

Materials and methods: Acquisitions on an image-quality phantom were performed using DSCT equipment with 100/Sn150 kVp for four dose levels (CTDIvol: 20/11/8/5mGy). Raw data were reconstructed for six energy levels (40/50/60/70/80/100 keV) using filtered back projection and two levels of ADMIRE (A3/A5). Noise power spectrum (NPS) and task-based transfer function (TTF) were calculated on virtual monoenergetic images (VMIs). Detectability index (d′) was computed to model the detection task of two enhanced iodine lesions as function of keV.

Results: Noise-magnitude was significantly reduced between 40 to 70keV by -56 ± 0 % (SD) (range: -56% – -55%) with FBP; -56 ± 0 % (SD) (-56% – -56%) with A3; and -57 ± 1 % (SD) (range: -57% – -56%) with A5. The mean spatial frequency of the NPS peaked at 70 keV and decreased as ADMIRE level increased. TTF values at 50% were greatest at 40 keV and shifted towards lower frequencies as the keV increased. The detectability of both lesions increased with increasing dose level and ADMIRE level. For the simulated lesion with iodine at 2 mg/mL, d’ values peaked at 70keV for all reconstruction types, except for A3 at 20 mGy and A5 at 11 and 20 mGy, where d’ peaked at 60 keV. For the other simulated lesion, d’ values were highest at 40 keV and decreased beyond.

Conclusion: At low keV on VMIs, this study confirms that iterative reconstruction reduces the noise magnitude, improves the spatial resolution and increases the detectability of enhanced iodine lesions.

Keywords: Multidetector computed tomography; Dual energy; Iterative reconstruction; Task-based image quality assessment; Phantom study.

Abbreviations

ADMIRE: Advanced modeled iterative reconstruction; CT: Computed tomography; $CTDI_{vol}$: Volume CT dose index; DECT: Dual-energy CT; FBP: Filtered back projection; HU: Hounsfield unit; IR: Iterative reconstruction; LSP: Line spread function; MBIR: Model-based iterative reconstruction; NPWE: Non-pre whitening matched filter with eye filter; NPS: Noise power spectrum; ROI: region of interest; SECT: Single-energy CT; SD: standard deviation; TTF: Task-based transfer function; VMI: Virtual monoenergetic image;

1. Introduction

Dual-energy CT (DECT) is widely used in clinical practice, especially for abdominal imaging [1-5]. DECT allows acquisition of the attenuation difference of various materials as a function of energy, which improves the detection and/or characterization of hepatic, pancreatic or renal lesions [2-7]. To obtain DECT images; low- and high-energy photon spectra were used to compute separately the photoelectric and Compton scattering effects [7]. Redistributing the ratio of these two effects in each voxel generates different types of images including virtual monoenergetic images (VMI).

Several DECT platforms exist to obtain both low- and high-energy photon spectra. A dual-source CT (DSCT) platform acquires image datasets using two X-ray tube/detector pairs (95°): one tube using low kVp (ranging from 70 to 100 kVp) and the other high kVp (140 or Sn150 kVp). Most clinical studies performed on patients for abdominal explorations on a DSCT platform have been carried out with the kVp pair 100/Sn 150 kVp [8-11]. Using this system, the tube current modulation system and iterative reconstruction (IR) could be used to optimize the doses delivered to patients, like for single-energy CT (SECT) acquisitions [12-16].

Several studies on phantoms and patients have evaluated the spectral performance of DSCT on filtered back projection (FBP) images using classical metrics such as the accuracy of Hounsfield units (HU) values and the iodine bias [17-20]. However, few studies have assessed the impact on the spectral performance of the dose reduction and the use of IR or model-based IR (MBIR) algorithms, such as advanced modeled iterative reconstruction (ADMIRE). This algorithm uses a probabilistic method, deriving a statistical cost function by incorporating X-ray physics and raw data statistical modeling to reduce noise and minimize artifacts [12]. Many clinical studies on SECT acquisitions have demonstrated that the use of this algorithm allows reducing the dose and/or the image noise for the same reconstruction time than for FBP images [12-14]. However, as for all IR and MBIR algorithms, the image texture is changed (*i.e.*, image smoothing), especially for high iterative levels, which can impede the radiologist interpretation and limits its use in clinical practice [12, 13].

A task-based image quality assessment is now commonly used for SECT acquisitions when IR algorithms are used [12-14, 21]. Recently, this method for DECT acquisitions was used to compare the impact of IR reconstruction on low-energy monochromatic images for a fast kV switching DECT system [22] and to compare the performance of four DECT platforms using a task-based image quality assessment [23]. This assessment uses metrics such as the noise power spectrum (NPS) to assess both the magnitude and texture of the noise; and the task-based transfer function (TTF) to evaluate the spatial resolution. A detectability index (d′) can then be computed to estimate the radiologist's ability to perform a clinical task [21, 24]. The d' value reflects the noise and resolution properties (NPS and TTF outcomes) related to the ability of the system to perform a task of interest.

The purpose of this study was to assess the impact of the dose reduction and the use of an advanced MBIR algorithm on low-energy monochromatic images by measuring noise characteristics, spatial resolution and detectability of two simulated lesions.

2. Materials and methods

2.1. Phantoms used

An elliptical (30 cm × 40 cm × 16.5 cm) multi-energy CT phantom model 1472 (Sun Nuclear) was used to assess the contrast between the soft tissue and the blood-mimicking material plus iodine at 2.0 mg/mL or at 4.0 mg/mL inserts. These inserts (diameter of 28.5 mm; placed in water equivalent as background material) were selected to represent tissues of anatomical structures present on enhanced abdominal CT examinations (**Figure 1**).

A 20-cm-diameter ACR QA phantom (Gammex 464) placed inside a body ring (diameter of 33 cm and length of 24 cm) was used to measure NPS and the TTF (**Figure 1**).

2.2. Acquisition and reconstruction parameters

Acquisitions were performed on a third generation of DECT (Somatom® Force, Siemens Healthineers). Acquisition parameters of classical abdomen-pelvic examination were used:100/Sn150 kVp, rotation time of 0.5 s/rot, pitch factor of 0.6, beam collimation of 128 × 0.6 mm. Tube currents (mAs) were adjusted to obtain four dose levels ($CTDI_{vol}$: 20, 11, 8 and 5 mGy) and the tube current modulation system was disabled.

Raw data were reconstructed using the standard soft tissue reconstruction kernel (Br40) usually used for abdomen-pelvic exploration and with the FBP, the level 3 and 5 of ADMIRE (A3; A5) corresponding to the intermediate level and highest level, respectively. Images were reconstructed with slice thickness close to 1 mm (1-mm increment) and a field of view of 250 mm for the ACR phantom and 420 mm for the multi-energy CT phantom.

2.3. Assessment of CT numbers

HU values were measured in a single slice positioned in the center of the multi-energy CT phantom, by semi-automatically placing one circular region of interest (ROI) with a diameter of 2 cm in the three selected inserts. For each insert, the N_{CT} (mean attenuation of pixels within each ROI) was computed for six energy levels (40/50/60/70/80/100 keV) on VMIs, using the “Monoenergetic +” application on the Syngo.Via software. The contrast between the soft tissue and each simulated contrast-enhanced blood inserts was computed for each energy level.

2.4. Task-based image quality assessment

Task-based image quality assessment was carried out using imQuest (Duke University) [24] to assess the noise texture and magnitude using NPS and the spatial resolution using the TTF [21, 24]. All metrics were computed on monochromatic images for the six energy levels (40/50/60/70/80/100 keV).

2.4.1. Noise power spectrum

NPS was computed by placing four square ROIs in the uniform section (module 3) of the ACR phantom (Figure 1.b), as follows:

$$NPS_{2D}(f_x, f_y) = \frac{\Delta_x \Delta_y}{L_x L_y} \frac{1}{N_{ROI}} \sum_{i=1}^{N_{ROI}} |FT_{2D}\{ROI_i(x,y) - \overline{ROI_\iota}\}|^2$$

where Δx and Δy are the pixel size in the x- and y-directions, respectively, Lx and Ly are the ROI size in pixels along the x and y axis, respectively, N_{ROI} is the number of ROIs, FT is the Fourier transform and $\overline{\mathrm{ROI}_\iota}$ is the mean pixel value measured from ROI(x, y) using a first-order detrending technique. The combined NPS was computed on 80 ROIs (N_{ROI}) of 128 ×128 pixels (L_x and L_y) each, from 20 consecutive axial slices.

To quantify the changes of magnitude and texture of noise between VMIs, the square root of the integral of the NPS curve and average spatial frequency (f_{av}) of the NPS curve were measured respectively.

2.4.2. Task-based transfer function

The TTF was assessed using acrylic insert available in module 1 of the ACR phantom from 10 consecutive axial slices according to the methodology previously reported [25]. A circular ROI was placed around the insert, and a circular-edge technique was employed to measure the edge spread function by plotting the HU value of each pixel as a function of the distance to the center of the insert. The line spread function was then obtained by derivation of the edge spread function. The TTF was computed from the normalized Fourier transformation of the line spread function.

2. 4. 3.Detectability indexes

A detectability index (d') was computed to assess the detection of simulated contrast enhanced abdominal lesions as function of dose levels, reconstruction type and energy levels. d' combines the noise (NPS) and resolution (TTF) properties of the images with a predefined function, noted Wtask, representative [21] of a clinical imaging task to estimate how well a human observer would perform the considered task.

This index was based on a non-prewhitening matched filter with eye filter (NPWE) model observer as:

$$d'^{2}_{NPWE} = \frac{\left[\iint |W(u,v)|^{2}.TTF(u,v)^{2}.E(u,v)^{2}dudv\right]^{2}}{\iint |W(u,v)|^{2}.TTF(u,v)^{2}.NPS(u,v)^{2}.E(u,v)^{4}dudv}$$

where u and v are the spatial frequencies in the x- and y-directions, E the eye filter that models the human visual system sensitivity to different spatial frequencies[24, 27], and W(u,v) the task function defined as:

$$W = |F\{h_1(x,y) - h_2(x,y)\}|$$

where $h_1(x,y)$and $h_2(x,y)$ correspond to the object present and the object absent hypotheses, respectively. The eye filter was modeled according to the visual response function [28].

Two task functions were defined to model the detection task of two circular contrast-enhanced lesions of 10-mm diameter. The contrast of each clinical task was defined directly from the N_{CT} variations between the soft tissue insert and the blood-mimicking material plus iodine at 2.0 mg/mL or at 4.0 mg/mL inserts, to take into account the N_{CT} variations as function of keV. The characteristics of these two simulated lesions could approach the contrast of a hepatocellular carcinoma during arterial phase or that of a hypervascularized metastasis.

The interpretation conditions used to obtain d’ included a 1.5 zoom factor, a viewing distance of 450 mm and a 500-mm field of view to refer to the visualization screen. For each detection task, the TTF and NPS were combined with the task function to estimate d’ for the six energy levels. d’ values obtained for these energy levels were compared with those obtained for a single energy CT acquisition at 120 kVp.

2. 5. Dosimetry

For all dose levels, the $CTDI_{vol}$ were measured using the 32-cm diameter reference phantom and a pencil ionization chamber (Xi CT detector, RaySafe). The ionization chamber was placed in the center of the phantom and then in each of the four cardinal peripheral positions. Three acquisitions were performed for each ionization chamber position and the $CTDI_{vol}$ were computed. The measured $CTDI_{vol}$ values were compared to the displayed values available from the CT workstation in the review report. The deviation between the $CTDI_{vol}$ measured and displayed for all CT systems used was lower than ±25% according to IEC 60601-2-44.

2. 6. Statistical analysis

Statistical analysis was performed using 'Biostatgv' (http://marne.u707.jussieu.fr/biostatgv). Quantitative variables were expressed as means ± standard deviation (SD) and ranges. Values of noise magnitude, noise texture (f_{av}), spatial resolution (f_{50}) and detectability (d’) obtained for all energy levels (keV) as function of dose level and reconstruction type were compared using the paired Mann-Whitney-Wilcoxon test. A *P*-value < 0.05 was considered to indicate significant differences.

3. Results

3.1. Contrast

Table 1 depicts the mean contrast between the soft tissue insert and the blood-mimicking material plus iodine at 2.0 mg/mL or at 4.0 mg/mL inserts as function of keV for all dose levels and reconstruction types. The highest values of contrast were found using the insert with iodine 4 mg/mL and differences between both inserts were greatest for lowest keV. Contrast values were similar for each keV irrespective of the dose level or reconstruction type.

3.2. Noise power spectrum

3.2.1. Noise magnitude

For all dose levels and reconstruction types, the noise magnitude decreased between 40 keV to 100 keV (**Figure 2.a**). Noise magnitude was reduced on average by -56 ± 1 (SD) % (range: -57 – 56%), whatever the reconstruction type.

Irrespective of the energy levels and the reconstruction types, noise magnitude was increased when the dose decreased. Noise magnitude was significantly increased on average by 21 ± 1 (SD) % (range: 18 – 23%) ($P < 0.001$) between 20 and 11 mGy; by 31 ± 1 (SD) % (range: 29 – 34%) ($P < 0.001$) between 20 and 8 mGy; and, 48 ± 4 (SD) % (range: 43 – 55%) ($P < 0.001$) between 20 and 5 mGy.

At all energy levels, the noise magnitude was inferior with IR and further decreased when increasing the level of ADMIRE. The noise reductions with ADMIRE compared to FBP were similar at all dose levels. Compared to FBP, noise magnitude was significantly reduced on average by -24 ± 1 (SD) % (range: -25 – -23%) ($P < 0.001$) with ADMIRE 3 and -45 ± 1 (SD) % (range: -47% – -42%) ($P < 0.001$) with ADMIRE 5.

3.2.2. Noise texture

For all dose levels and reconstruction types, the average NPS spatial frequency (NPS_{fav}) was greatest at 70 keV (**Figure 2.b**). NPS_{fav} shifted towards higher frequencies from 40 to 70 keV and shifted towards lower frequencies from 70 to 100 keV.

For all energy levels, NPS_{fav} shifted towards lower frequencies when the dose level decreased and the iterative level increased. NPS_{fav} was significantly reduced on average by -3 ± 1 (SD) % (range: -4% – -2%) ($P < 0.001$) between 20 and 11 mGy; by -6 ± 1 (SD) % (range: -8 – -5%) ($P < 0.001$) between 20 and 8 mGy; and -12 ± 1 (SD) % (range: -13 – -10%) ($P < 0.001$) between 20 and 5 mGy. Compared to FBP, NPS_{fav} was significantly reduced on average by -9 ± 1 (SD) % (range: -11 – -8%) ($P < 0.001$) with ADMIRE 3 and -22 ± 2 (SD) % (range: -26 – -19%) ($P < 0.001$) with ADMIRE 5.

3.3. Task transfer function

The values of TTF at 50% (f_{50}) shifted towards lower frequencies as the energy levels increased and the dose decreased (**Figure 3**). Between 20 and 11 mGy, f_{50} were decreased by -6 ± 6 (SD) % (range: -14 – 0%) ($P = 0.06$) with FBP, by -11 ± 4 (SD) % (range: -14 – -2%)

(*P* = 0.035) with A3 and -17 ± 8 (SD) % (range: -23 – -3%) (*P* = 0.035) with A5 and -14 ± 4% (SD) (range: -19 – -9%) (*P* = 0.035), -23 ± 3 (SD) % (range: -29 – -20%) (*P* = 0.035), -31 ± 6 (SD) % (range: -40 – -24%) (*P* = 0.035) between 20 and 5 mGy, respectively.

Similar values of f_{50} were found as function of energy levels for 5 mGy for all reconstruction types (*P* = 0.27 between FBP and ADMIRE 3 and *P* = 0.44 between FBP and ADMIRE 5). Greater values of f_{50} were found with ADMIRE 3 followed by with ADMIRE 5 compared to FBP at 40 keV for 8 mGy and at 40, 50 and 60 keV for 11 mGy. Compared to FBP for 20 mGy, greater f_{50} values were found for ADMIRE 3 (14 ± 5 [SD] %; range: 6 – 19%) *(P* = 0.035*)* and for ADMIRE 5 (28 ± 8 [SD] %; range: 15 – 34%) (*P* = 0.035).

3.4. Detectability index

Figure 4 shows the d' obtained for the two simulated lesions as function of the energy level for each dose level and reconstruction type. The d' values were higher for the lesion with an iodine concentration at 4 mg/mL.

The detectability of both lesions increased as the dose level and the iterative level increased (**Table 2**). For both lesions, d' was significantly decreased on average by -21 ± 3 (SD) % (range: -31 – -15%) (*P* < 0.001) between 20 and 11 mGy; by -31 ± 3 (SD) % (range: -40 – -25%) (*P* = 0.002) between 20 and 8 mGy; and by -42 ± 3% (SD) (range: -49 – -39%) (*P* < 0.001) between 20 and 5 mGy. Compared to FBP, d' was significantly increased on average by 19 ± 4 (SD) % (range: 14 – 32%) (*P* < 0.001) with ADMIRE 3 and by 42 ± 7 (SD) % (range: -31– 62%) (*P* < 0.001) with ADMIRE 5.

d' values as function of energy levels varied according to the simulated lesion. For the lesion at 2 mg/mL iodine, d' increased by 40 keV at an inversion point and then decreased thereafter (**Figure 4.a**). This reversal point was different depending on the dose level and the type of reconstruction. With FBP, d' peaked at 70 keV for all dose levels. With ADMIRE 3, d' peaked at 70 keV for 5, 8 and 11 mGy and peaked at 60 keV for 20 mGy. With ADMIRE 5, d' peaked at 70 keV for 5 and 8 mGy and peaked at 60 keV for 11 and 20 mGy. For the lesion at 4 mg/mL iodine, d' decreased as the dose increased for all dose levels and reconstruction type, except between 50 and 60 keV for A5 at 20 mGy (**Figure 4.b**).

d' values measured at energy levels ranging from 80 to 90 keV were greater than those obtained at 120 kVp for the lesion at 2 mg/mL iodine, and were greater from 70 to 80 keV for the lesion at 4 mg/mL iodine. Compared to FBP at 11 mGy (**Table 2**), d' values were significantly greater at 8 mGy with ADMIRE3 ([7 ± 3 (SD) %; range: 5 – 14%] at 2 mg/mL; *P* = 0.03) and [3 ± 3 (SD) %; range: 0 – 8%] at 4 mg/mL; *P* = 0.01) and with ADMIRE 5 ([26 ± 4 (SD) %; range: 21 – 34%] at 2 mg/mL; *P* = 0.03) and [21 ± 5 (SD) %; range: 15 – 28%] at 4 mg/mL; *P* = 0.03) but were in the same range at 5 mGy with ADMIRE 5 ([2 ± 4 (SD) %; range: -2 – 8%] at 2 mg/mL; *P* = 0.25) and ([0 ± 5 (SD) %; range: -10 – 3%] at 4 mg/mL; *P* = 0.59).

4. Discussion

This study demonstrates that the use of an advanced MBIR algorithm on virtual monoenergetic images reduced the noise magnitude but shifted towards lower frequencies the spatial resolution and the average NPS spatial frequency, which changes the image texture. The detectability of two simulated lesions was improved as the level of MBIR and the dose increased and favored the use of low energy level on VMI.

For a given energy level, our NPS results were similar to those previously found on SECT acquisitions [12, 13]. The image noise (NPS peak) decreased as the dose level increased and the level of ADMIRE increased. The average spatial frequency of the NPS shifted towards lower frequencies as the ADMIRE level increased and the dose level decreased, which results in a modification of the image texture such as its smoothing [12, 14, 21]. On VMIs, we found that the highest image noise levels were found at 40 keV and decreased afterwards, especially from 40 to 70 keV. As previously defined, “these results were related to the anti-correlation of the noise in the basis material images used to calculate the VMIs by linear combination” [20]. Our results also showed that the average spatial frequency of the NPS (NPS f_{av}) peaked at 70 keV and shifted towards lower frequency from 70 to 40 keV and from 70 to 100 keV. Similar NPS outcomes as a function of keV on VMIs were found for a fast kV switching DECT system with another IR algorithm (ASIR) [22] and for the same DECT system with the FBP and the 80/Sn150 kVp pair [23].

Our TTF outcomes show that the highest values of f_{50} were found for 40 keV and f_{50} shifted towards lower frequencies as keV increased, reducing the spatial resolution. For a given energy level, we found that TTF decreased as the dose decreased. The impact of ADMIRE on TTF outcomes differed as function of keV and dose level. The more the dose level increased, the greater the impact on f_{50} between the levels of ADMIRE and the FBP increased. At 5 mGy, similar values of f_{50} were found for all reconstruction types. However, at 20 mGy, f_{50} for A3 were 14 ± 5 (SD) % and greater than the FBP and 28 ± 8 (SD) % for

A5. For both other dose levels, f_{50} differences between FBP and ADMIRE levels were only found at 40 and 50 keV. Similar results in terms of variations of f_{50} as function of keV on VMIs were found [19,20].

The detectability index results showed that d′ values increased when the dose and the level of ADMIRE increased, regardless the energy level used. Similar results were found with ADMIRE on SECTs for one energy level [12-14]. The variations of d’ values as function of keV differed according to the simulated lesion and were directly correlated to their contrast variations. Indeed, the calculation of d 'depends on three components: one related to the performance of the CT system used (NPS and TTF outcomes); one linked to the observer (condition of interpretation); and the last related to the definition of the specific clinical task assessed. For the latter, it is necessary to define a lesion to be detected by specifying its size, shape and contrast. For the simulated lesion with an iodine concentration at 4 mg/mL, the photoelectric effect was then predominant and the contrast was high. The variations in the contrast of this lesion as a function of the keV strongly influenced the values of d', unlike the NPS and TTF outcomes. d’ values peaked at 40 keV and decreased beyond. The curves of d' values as function of keV followed the same trend as the contrast curves. For the other simulated lesion with iodine at 2 mg/mL, the contrast values and their variation as a function of keV were weaker. d’ values were therefore more influenced by NPS and the TTF outcomes than by the contrast variation. With a lower noise magnitude and higher NPS f_{av} values, d’ values peaked at 70 keV for the FBP for all dose levels. However, using ADMIRE, the d’ values tended to shift towards lower keV when the dose level increased and the level of ADMIRE increased. At 20 mGy, d’ values peaked at 60 keV but peaked at 70 keV for 5 mGy. In all cases, for energy levels lower than 70 keV, d’ values of both simulated lesions were higher than those obtained at 120 kVp.

In this study we found that the use of ADMIRE reduced the image noise, improved the detectability and favored the use of low keV for the detection of enhanced iodine lesions. As for SECT acquisitions, ADMIRE could also be used to optimize and reduce the dose delivered to the patient. ADMIRE reduced the dose level by maintaining a sufficient image quality compared to FBP images. The dose reduction was greater with the highest ADMIRE level. However, as for SECT acquisitions, the use of highest ADMIRE level changed the image texture for a given energy level and these changes in texture increase for the lowest energy level. A further patient study on abdominal imaging could be performed to assess if the change in image texture using ADMIRE for lower dose levels impedes the radiologist’s interpretation on VMIs images at low keV. Finally, the task-based image quality assessment used in the present study could be extended to assess the spectral performance of new photon counting CT systems [29] and new deep learning image reconstruction algorithms now available on some DECT platforms [30, 31].

This study has several limitations. Acquisitions were performed for a single standard reconstruction kernel and for one of the five kVp pairs available on this DSCT. Also, the use of other parameters combinations may show different outcomes. For the study, two task functions were chosen to model the detection of contrast-enhanced lesions. The contrast of these lesions was defined according to the N_{CT} variations as function of keV for two inserts available in the multi-energy CT phantom. This method was chosen to take into account the variation in contrast of both simulated lesions according to energy level. However, a clinical study on known lesions, with a specific size and contrast-enhanced, should be carried out to confirm these results.

In conclusion, this study demonstrated that using ADMIRE at low-energy on VMIs could limit the increase of the noise magnitude and improve spatial resolution. Hence, it could enhance detectability of enhanced iodine lesions at low keV on VMIs. The parametric results analyzed on phantom should be validated in clinical practice for the detection and/or characterization of abdominal lesions at for low keV on VMIs.

Acknowledgments

We thank S. Kabani for her help in editing the manuscript.

Human rights

This study was performed with phantoms and did not involve human subjects

Informed consent and patient details

Institutional review board approval was not needed because this study was performed with phantoms and did not involve human subjects

Disclosure of interest

The authors declare that they have no competing interest.

Funding

This study did not receive specific fundings.

Author contributions

All authors attest that they meet the current International Committee of Medical Journal Editors (ICMJE) criteria for Authorship.

References

1 Agrawal MD, Pinho DF, Kulkarni NM, Hahn PF, Guimaraes AR, Sahani DV. Oncologic applications of dual-energy CT in the abdomen. Radiographics 2014; 34:589–612.

2 De Cecco CN, Schoepf UJ, Steinbach L, Boll DT, Fole, WD, Kaza RK, et al. White paper of the Society of Computed Body Tomography and Magnetic Resonance on dual-energy CT, Part 3: vascular, cardiac, pulmonary, and musculoskeletal applications. J Comput Assist Tomogr 2017; 41:1–7.

3 Marin D, Boll DT, Mileto A, Nelson RC. State of the art: dual-energy CT of the abdomen. Radiology 2014; 271:327–42.

4 Karcaaltincaba M, Aktas A. Dual-energy CT revisited with multidetector CT: review of principles and clinical applications. Diagn Interv Radiol 2011; 17:181–94.

5 Jamali S, Michoux N, Coche E, Dragean CA. Virtual unenhanced phase with spectral dual-energy CT: Is it an alternative to conventional true unenhanced phase for abdominal tissues? Diagn Interv Imaging 2019; 100:503–11.

6 McCollough CH, Leng S, Yu L, Fletcher JG. Dual- and multi-energy CT: principles, technical approaches, and clinical applications. Radiology 2015; 276:637–53.

7 Alvarez RE, Macovski A. Energy-selective reconstructions in X-ray computerized tomography. Phys Med Biol 1976; 21:733–44.

8 Hardie AD, Picard MM, Camp ER, Perry JD, Suranyi P, De Cecco CN, et al. Application of an advanced image-based virtual monoenergetic reconstruction of dual Source dual-energy CT Data at Low keV increases image quality for routine pancreas imaging. J Comput Assist Tomogr 2015; 39:716–20.

9 Caruso D, De Cecco CN, Schoepf UJ, Schaefer AR, Leland PW, Johnson D, et al. Can dual-energy computed tomography improve visualization of hypoenhancing liver lesions in portal venous phase? Assessment of advanced image-based virtual monoenergetic images. Clin Imaging 2017; 41:118–124.

10 De Cecco CN, Caruso D, Schoepf UJ, Wichmann JL, Ter Louw JR, Perry JD, et al. Optimization of window settings for virtual monoenergetic imaging in dual-energy CT of the liver: a multi-reader evaluation of standard monoenergetic and advanced imaged-based monoenergetic datasets. Eur J Radiol 2016; 85:695–9.

11 De Cecco CN, Muscogiuri G, Schoepf UJ, Caruso D, Wichmann JL, Cannao PM, et al. Virtual unenhanced imaging of the liver with third-generation dual-source dual-energy CT and advanced modeled iterative reconstruction. Eur J Radiol 2016; 85:1257–64.

12 Greffier J, Frandon J, Larbi A, Beregi JP, Pereira F. CT iterative reconstruction algorithms: a task-based image quality assessment. Eur Radiol 2020; 30:487–500.

13 Greffier J, Frandon J, Pereira F, Hamard A, Beregi JP, Larbi A, et al. Optimization of radiation dose for CT detection of lytic and sclerotic bone lesions: a phantom study. Eur Radiol 2020; 30:1075–8.

14 Greffier J, Larbi A, Frandon J, Moliner G, Beregi JP, Pereira F. Comparison of noise-magnitude and noise-texture across two generations of iterative reconstruction algorithms from three manufacturers. Diagn Interv Imaging 2019; 100:401–10.

15 Laurent G, Villani N, Hossu G, Rauch A, Noel A, Blum A, et al. Full model-based iterative reconstruction (MBIR) in abdominal CT increases objective image quality, but decreases subjective acceptance. Eur Radiol 2019; 29:4016–25.

16 Martini K, Moon JW, Revel MP, Dangeard S, Ruan C, Chassagnon G. Optimization of acquisition parameters for reduced-dose thoracic CT: a phantom study. Diagn Interv Imaging 2020; 101:269–79.

17 Jacobsen MC, Cressman ENK, Tamm EP, Baluya DL, Duan X, Cody DD, et al. Dual-energy CT: lower limits of iodine detection and quantification. Radiology 2019; 292:414–9.

18 Jacobsen MC, Schellingerhout, D, Wood, CA, Tamm, EP, Godoy, MC, Sun, J, et al. Intermanufacturer comparison of dual-energy CT iodine quantification and monochromatic attenuation: a phantom study. Radiology 2018; 287:224–34.

19 Euler A, Parakh A, Falkowski AL, Manneck S, Dashti D, Krauss B, et al. Initial results of a single-source dual-energy computed tomography technique using a split-filter: assessment of image quality, radiation dose, and accuracy of dual-energy applications in an in vitro and in vivo study. Invest Radiol 2016; 51:491–8.

20 Sellerer T, Noel PB, Patino M, Parakh A, Ehn S, Zeiter S, et al. Dual-energy CT: a phantom comparison of different platforms for abdominal imaging. Eur Radiol 2018; 28:2745–55.

21 Same E, Richard S. Assessment of the dose reduction potential of a model-based iterative reconstruction algorithm using a task-based performance metrology. Med Phys 2015; 42:314–23.

22 Greffier J, Frandon J, Hamard, A, Teissier, JM, Pasquier, H, Beregi, JP, et al. Impact of iterative reconstructions on image quality and detectability of focal liver lesions in low-energy monochromatic images. Phys Med 2020; 77:36–42.

23 Greffier J, Si-Mohamed S, Dabli D, de Forges H, Hamard A, Douek P, et al. Performance of four dual-energy CT platforms for abdominal imaging: a task-based image quality assessment based on phantom data. Eur Radiol 2021, 10.1007/s00330-020-07671-2.

24 Samei E, Bakalyar D, Boedeker KL, Brady S, Fan J, Leng S, et al. Performance evaluation of computed tomography systems: summary of AAPM Task Group 233. Med Phys 2019; 46:e735–56.

25 Richard S, Husarik DB, Yadava G, Murphy SN, Samei E. Towards task-based assessment of CT performance: system and object MTF across different reconstruction algorithms. Med Phys 2012; 39:4115–22.

26 Greffier J, Boccalini S, Beregi JP, Vlassenbroek A, Vuillod A, Dupuis-Girod S, et al. CT dose optimization for the detection of pulmonary arteriovenous malformation (PAVM): a phantom study. Diagn Interv Imaging 2020; 101:289–97.

27 Burgess AE, Li X, Abbey CK. Visual signal detectability with two noise components: anomalous masking effects. J Opt Soc Am A Opt Image Sci Vis 1997; 14:2420–42.

28 Eckstein M, Bartroff J, Abbey C, Whiting J, Bochud F. Automated computer evaluation and optimization of image compression of X-ray coronary angiograms for signal known exactly detection tasks. Opt Express 2003; 11:460–75.

29 Si-Mohamed S, Boccalini S, Rodesch PA, Dessouky R, Lahoud E, Broussaud T, et al. Feasibility of lung imaging with a large field-of-view spectral photon-counting CT system. Diagn Interv Imaging 2021; doi: 10.1016/j.diii.2021.01.001.

30 Singh R, Digumarthy SR, Muse VV, Kambadakone AR, Blake MA, Tabari A, et al. Image quality and lesion detection on deep learning reconstruction and iterative reconstruction of submillisievert chest and abdominal CT. AJR Am J Roentgenol 2020; 214:566–73.

31 Greffier J, Hamard A, Pereira F, Barra C, Pasquier H, Beregi JP, et al. Image quality and dose reduction opportunity of deep learning image reconstruction algorithm for CT: a phantom study. Eur Radiol 2020; 30:3951–9.

Figure legends

Figure 1. a. Figure shows virtual monochromatic image at 70 keV of multi-energy CT phantom with position of soft tissue and blood-mimicking material plus iodine at 2.0 mg/mL and 4.0 mg/mL inserts used for the assessment of HU precision; b. Figure shows four regions of interest (ROIs) of 128 × 128 pixels used for the noise power spectrum (NPS) assessment delineated by blue lines; c. Figure shows ROIs used to compute the task-based transfer function (TTF) placed on the acrylic insert.

Figure 2. Graphs show values of noise magnitude (a) and mean noise power spectrum (NPS) spatial frequency (f_{av}; b) according to energy levels for all dose levels and the filtered back projection (FBP) and the two levels of ADMIRE.

Figure 3. Graphs show values of task-based transfer function at 50% (f_{50}) obtained for the acrylic insert according to the energy level for all dose levels and the filtered back projection (FBP) and the two levels of ADMIRE.

Figure 4. Graphs show detectability index (d') for the detection tasks of two contrast-enhanced lesions according to the energy level for all dose levels and the filtered back projection (FBP) and the two levels of ADMIRE. Simulated lesions with characteristics of contrast corresponding to the soft tissue and blood mimicking iodine at 2 mg/mL (a) and the soft tissue and blood mimicking iodine at 4 mg/mL (b) are presented.

Table 1. Mean contrast between the soft tissue insert and the blood-mimicking material plus iodine obtained for all reconstruction type used and for all dose levels.

Table 2. Detectability index (d') values for the detection tasks of two contrast-enhanced lesions (2 mg/mL and 4mg/mL) according to the energy level for all dose levels and filtered back projection (FBP) and two levels of ADMIRE.

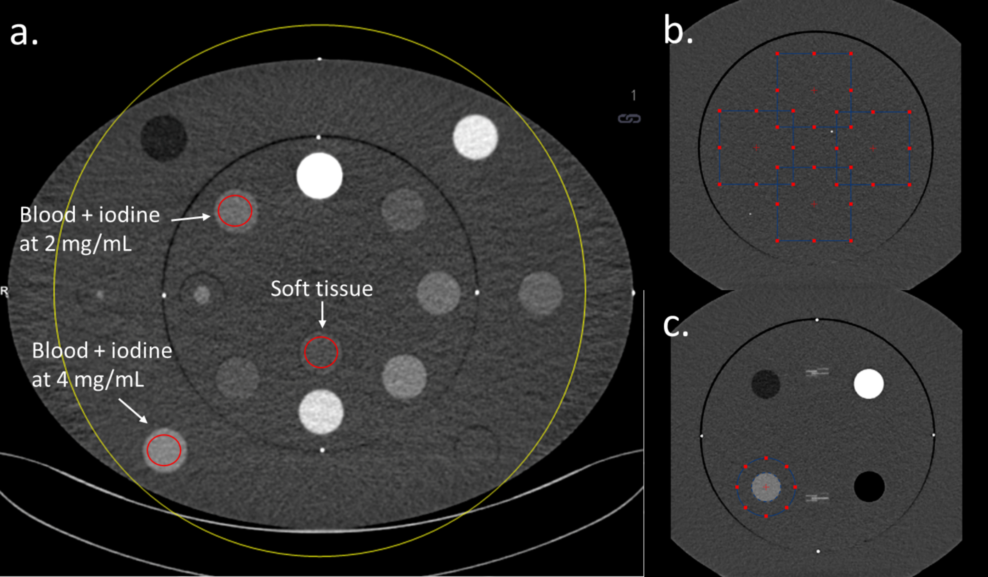
a.
b.
c.
Blood + iodine at 2 mg/mL
Soft tissue
Blood + iodine at 4 mg/mL
R
1

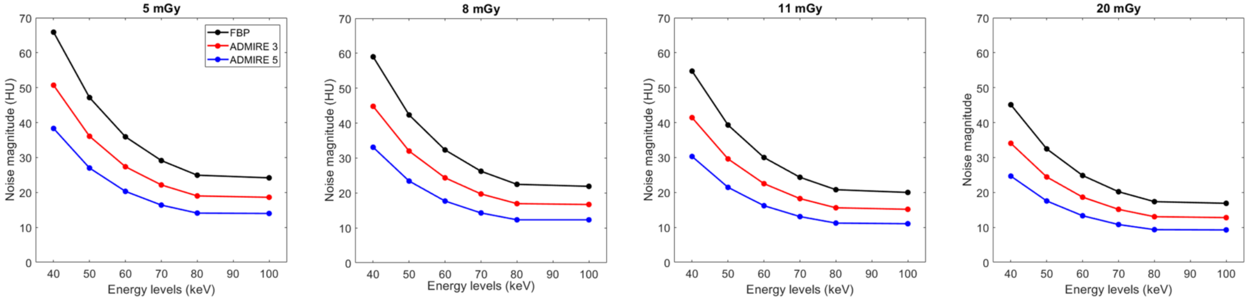
5 mGy
8 mGy
11 mGy
20 mGy
FBP
ADMIRE 3
ADMIRE 5
Noise magnitude (HU)
Noise magnitude
Energy levels (keV)
0
10
20
30
40
50
60
70
40
50
60
70
80
90
100

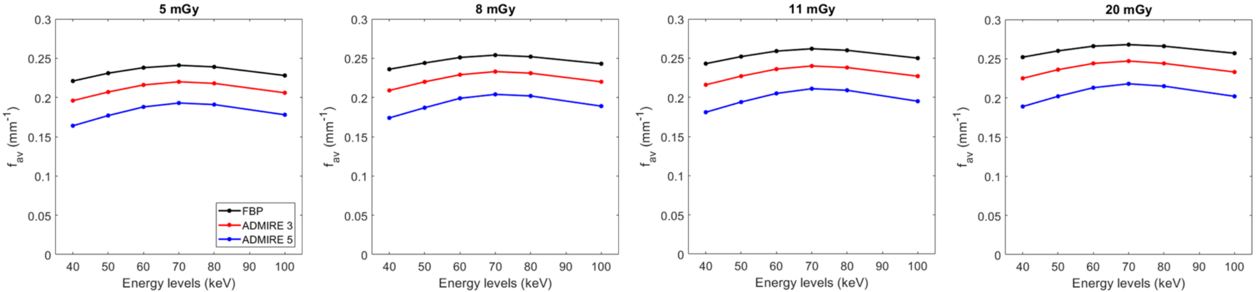
5 mGy
8 mGy
11 mGy
20 mGy
f_{av} (mm^{-1})
0.3
0.25
0.2
0.15
0.1
0.05
0
40
50
60
70
80
90
100
Energy levels (keV)
FBP
ADMIRE 3
ADMIRE 5

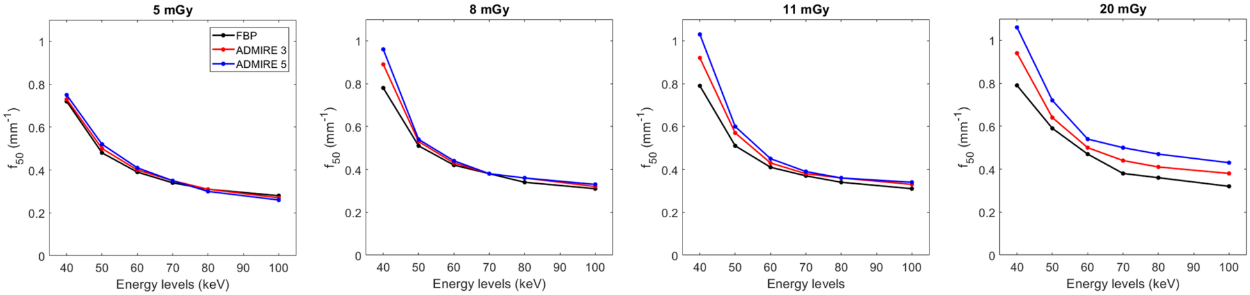
5 mGy
8 mGy
11 mGy
20 mGy
FBP
ADMIRE 3
ADMIRE 5
f_{50} (mm^{-1})
0
0.2
0.4
0.6
0.8
1
40
50
60
70
80
90
100
Energy levels (keV)
Energy levels

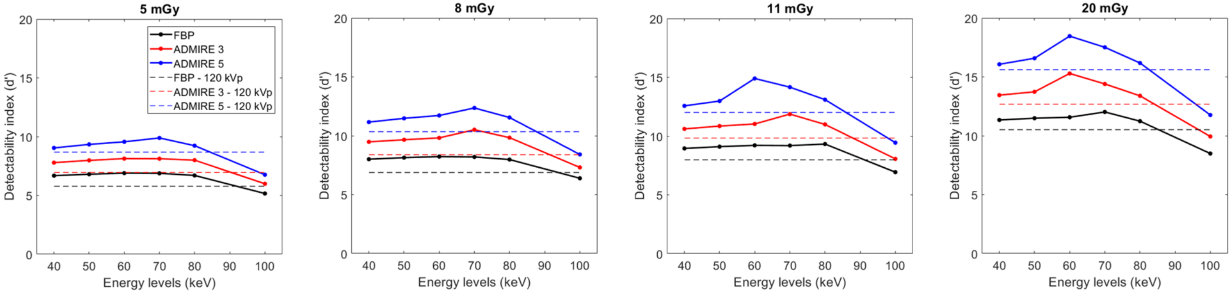
5 mGy
8 mGy
11 mGy
20 mGy
FBP
ADMIRE 3
ADMIRE 5
FBP - 120 kVp
ADMIRE 3 - 120 kVp
ADMIRE 5 - 120 kVp
Detectability index (d')
0
5
10
15
20
Energy levels (keV)
40
50
60
70
80
90
100

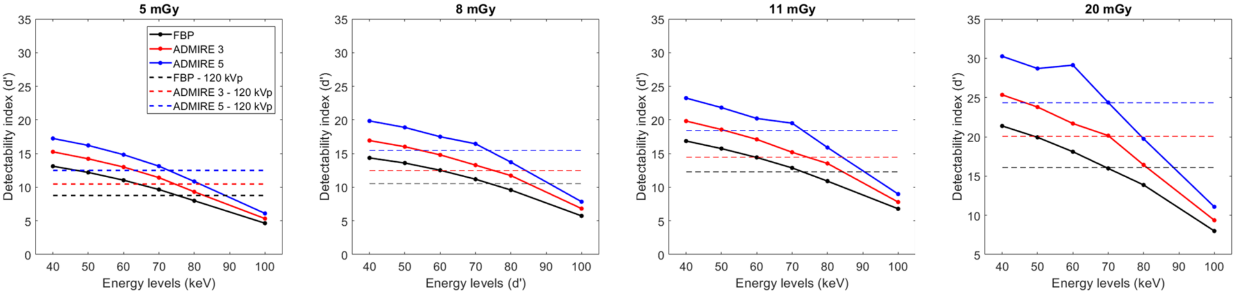
5 mGy
8 mGy
11 mGy
20 mGy
FBP
ADMIRE 3
ADMIRE 5
FBP - 120 kVp
ADMIRE 3 - 120 kVp
ADMIRE 5 - 120 kVp
Detectability index (d')
0
5
10
15
20
25
30
35
40
50
60
70
80
90
100
Energy levels (keV)
Energy levels (d')
Energy levels (keV)
Energy levels (keV)

	Contrast between soft tissue and blood-mimicking material plus iodine at	
	2 mg/mL	4 mg/mL
40 keV	223.2 ± 14.6 [210–244]	421.5 ± 15.8 [402–422]
50 keV	159.4 ± 8.3 [152–171]	277.0 ± 8.5 [266–288]
60 keV	120.7 ± 4.6 [116–127]	189.1 ± 4.1 [184–195]
70 keV	96.7 ± 2.3 [94–100]	134.9 ± 1.4 [133–137]
80 keV	81.5 ± 1.2 [80–83]	100.5 ± 0.8 [99–102]
100 keV	61.7 ± 1.5 [59–64]	64.3 ± 1.7 [62–66]
120 kVp	83.2 ± 1.5 [82–27]	126.9 ± 3.0 [125–130]

Values are expressed in Hounsfield units as means ± standard deviations; numbers in brackets are ranges.

		d' soft tissue and blood mimicking iodine at 2 mg/mL			d' soft tissue and blood mimicking iodine at 4 mg/mL		
CTDI$_{vol}$ (mGy)	Energy levels (keV)	FBP	ADMIRE 3	ADMIRE 5	FBP	ADMIRE 3	ADMIRE 5
5	40	6.7	7.8	9.0	13.1	15.3	17.2
	50	6.8	8.0	9.3	12.2	14.2	16.2
	60	6.9	8.1	9.6	11.0	13.0	14.8
	70	6.9	8.1	9.9	9.7	11.4	13.1
	80	6.7	8.0	9.2	8.0	9.3	10.9
	100	5.2	6.0	6.8	4.7	5.3	6.1
8	40	8.0	9.5	11.2	14.4	16.9	19.9
	50	8.1	9.7	11.5	13.6	16.0	18.9
	60	8.2	9.8	11.7	12.5	14.8	17.5
	70	8.2	10.5	12.4	11.2	13.3	16.5
	80	8.0	9.8	11.6	9.6	11.7	13.7
	100	6.4	7.3	8.4	5.7	6.8	7.8
11	40	9.0	10.6	12.6	16.9	19.8	23.2
	50	9.1	10.9	13.0	15.7	18.6	21.8
	60	9.2	11.0	14.9	14.4	17.1	20.2
	70	9.2	11.9	14.2	12.9	15.2	19.5
	80	9.3	11.0	13.1	10.9	13.5	15.9
	100	6.9	8.1	9.4	6.8	7.8	9.0
20	40	11.3	13.5	16.1	21.4	25.3	30.2
	50	11.5	13.7	16.6	19.9	23.8	28.7
	60	11.6	15.3	18.5	18.1	21.7	29.1
	70	12.0	14.4	17.5	16.0	20.1	24.4
	80	11.2	13.4	16.2	13.9	16.4	19.7
	100	8.5	9.9	11.8	8.0	9.4	11.1

FBP: filtered back projection.